NASA Technical Memorandum 104007

Linear and Nonlinear Pattern Selection in Rayleigh-Benard Stability Problems

Sanford S. Davis, Ames Research Center, Moffett Field, California

May 1993

National Aeronautics and
Space Administration

Ames Research Center
Moffett Field, California 94035-1000

Summary

A new algorithm is introduced to compute finite-amplitude states using primitive variables for Rayleigh-Benard convection on relatively coarse meshes. The algorithm is based on a finite-difference matrix-splitting approach that separates all physical and dimensional effects into one-dimensional subsets. The nonlinear pattern selection process for steady convection in an air-filled square cavity with insulated side walls is investigated for Rayleigh numbers up to 20,000. The heated lower boundary is augmented with "noisy" boundary conditions to illustrate the transient and bimodal nature of the pattern selection process above the first critical Rayleigh number. Above a second critical Rayleigh number other instability modes may also be excited. The internalization of disturbances that evolve into coherent patterns is investigated and transient solutions from linear perturbation theory are compared with and contrasted to the full numerical simulations.

The basins of attraction for transient solutions in a phase plane are shown to be bounded by singular states representing unstable modes. A particular symmetric mode that may be stable to symmetric or random disturbances but unstable to antisymmetric disturbances is investigated.

Introduction

Rayleigh-Benard convection is considered by many an ideal model for hydrodynamic stability since convection and dissipation compete with one another in a relatively straightforward manner. Among the many proposed approximations to the Navier-Stokes equations, the simplified form first advocated by Boussinesq as a model of natural convection is now commonly used as the basis for most theoretical and numerical stability research. The classical solution method of linearization and expansion in sinusoidal functions as described in detail by Chandrasekhar (1961) is a firmly established tool for virtually all stability problems. The eigenvalue problem that determines the normal modes and critical parameters (in this case the Rayleigh number) is itself quite a difficult mathematical problem. In the continual search for simpler formulations, series expansions in terms of orthogonal functions other than sinusoids have been used with some success. In a recent study, Lee et al. (1989) used an expansion in Chebyshev polynomials to consider the linear stability of Rayleigh-Benard convection in a general two-dimensional cavity. The first instability mode is a single roll creating a vortex-type motion for cavities with aspect ratio less than two. The computed critical Rayleigh number for these finite-aspect-ratio cavities is well above the value 1708, which is appropriate for infinite-aspect-ratio systems. The normal mode approach to the perturbation equations will give eigenfunctions and eigenvalues but will not yield any other information, such as the sense of the induced flow, the nature of the transient motion, or the strength of the steady convecting state.

Finite-amplitude nonlinear steady convection at supercritical Rayleigh numbers has been addressed in the literature for many decades. A common approach is to use a Fourier series expansion to compute the final steady convective flow. The theoretical and experimental literature to 1980 has been reviewed by Busse (1981). In particular, a few investigators attempted to track the evolution of discrete modes as the solution to an initial-value problem. Saltzman (1962) was apparently the first to solve the nonlinear amplitude equations in an infinite horizontal layer and also to investigate the nature of the steady-state nonlinear modes. Ogura and Yagihashi (1969), using a similar approach, found that initial conditions played a key role in determining the ultimate steady-state pattern. In a later paper Ogura (1971) investigated the effect of a variety of initial conditions (in the context of Fourier modes) on the final steady state. This study showed that the flow may evolve through a series of patterns before the final state is achieved and that the then-conventional rule that the final steady-state flow corresponded to the flow with maximum Nusselt number was false.

In a recent and comprehensive work of this type, Goldhirsch et al. (1989) investigate natural convection in a rectangular enclosure by using Chebyshev expansions in the spatial coordinates and a time-split approach to the temporal coordinate. The flow is induced by a time-dependent exponential heating from below. The flow evolves by creating rolls at the boundaries that ultimately migrate into the cavity.

In the present paper, a new finite-difference approach is used to solve the Boussinesq equations in primitive variables. The method is based on a "discrete dispersion relation" approach to the convective terms and a new splitting algorithm to construct compact implicit finite-difference formulas. The technique is used to examine the pattern selection process where finite-amplitude steady solutions are known to exist. Realistic boundary and initial conditions, consisting of insulated side walls and prescribed temperatures on the top and bottom walls, are imposed. A unit step in temperature along with "noisy" lower-wall boundary conditions are used to initiate the motion. The general flow features outlined by Goldhirsh et al. (1989) are confirmed by using the current finite-difference approach, but certain details of the instability growth differ because of the use of insulated side walls, which induce a different set of eigenfunctions.

The same finite-difference algorithm is used to correlate stability boundaries predicted by the classical perturbation method. The most (linearly) unstable mode is computed by treating the perturbed Boussinesq equations as a transient stability problem. The eigenvalues and eigenfunctions, which appear as a natural outcome of the transient solution, are compared with direct solutions to the nonlinear equations. Numerical experiments in which the linear perturbation equations were used uncovered two instability modes over the range of Rayleigh numbers considered. Eigenfunctions from the linearized equations are also correlated with corresponding patterns computed during the nonlinear exponential growth and the finite-amplitude phases. The linearized solution is shown to dominate the flow evolution during the exponential growth phase, but it naturally fails to predict the ultimate nonlinear saturation.

Numerically generated steady-state solutions confirm results from finite-amplitude theory and a parabolic bifurcation emerges from the simulation. A series of computations with noisy boundary conditions illustrates the role of transients in the pattern selection process. It is found that the final pattern is imprinted at an early stage of the flow where linearly unstable modes first become dominant. If two modes are possible, there is a chance that either may be activated. When a symmetric mode is generated it may be transformed to a stable rotational mode if both the amplitude and the symmetry of imposed disturbances are consistent with this pattern. Above the second critical Rayleigh number the three possible modes are clockwise or counterclockwise rotational modes and one symmetric mode consisting of two counterrotating vortices with a central updraft.

Solutions to the Boussinesq equations are presented 1) as an example of a relatively complex fluid model to validate partially the algorithmic approach, 2) as a vehicle to examine some important physical effects, and 3) as a means of assessing the impact of linear theory on nonlinear processes. Primitive variables are chosen so that fully three-dimensional problems can be computed with the same algorithm. In this report the equations of free convection are reviewed; the new finite-difference approach is described; numerical solutions are presented in terms of integrated quantities and instantaneous velocity-temperature fields; and finally, the process by which small disturbances are internalized is examined by using instantaneous snapshots of the flow during a critical time interval and comparing with a simple second-order dynamical systems model. The numerical algorithm used to simulate the flow is described in the appendix.

The author would like to acknowledge the helpful discussions with Murray Tobak and Chris Hill regarding interpretation of the simulated flows.

Nomenclature

a	convection speed
cn	Courant number, $a\tau/h$
c_p	specific heat at constant pressure
dn	diffusion number
d	length scale
e	energy
$\vec{g}$	gravity vector
h	space increment
k	wavenumber in x-direction
l	wavenumber in y-direction
Pr	Prandtl number, ν/χ
$\vec{q}$	heat flux vector
Ra	Rayleigh number, $\beta g \Delta T d^3/\nu\chi$
Ra_c	critical Rayleigh number
T	temperature
t	time
U	energy
$\vec{v}$	velocity vector
α	eigenvalue (growth rate)
β	coefficient of thermal expansion
θ	temperature increment
ν	kinematic viscosity
ρ	density
τ	time increment
ω	radian frequency
χ	thermal diffusivity, $k/\rho_o c_p$

Formulation of Equations and Solution Method

Equations of Free Convective Flows

The Boussinesq equations result from the following assumptions regarding the Navier Stokes and Energy equations for an incompressible fluid: 1) Fourier's Law for an isotropic, homogeneous medium relates the heat

flux vector to the temperature gradient by $\vec{q} = -k\nabla T$; 2) imposed temperature differences do not invoke large density changes; and 3) the thermodynamic state variables (density and energy) depend only on the temperature. Since the pressure is not considered a thermodynamic state variable, the pressure term in the equations of motion is considered a "hydrodynamic" quantity only. Density and energy changes induced by temperature fluctuations are computed from the equations $\rho - \rho_0 = -\beta\rho_0(T - T_0)$ and $e - e_0 = c_p(T - T_0)$, where the constants are the coefficient of thermal expansion (β) and the specific heat at constant pressure (c_p).

With these assumptions, the equations of motion become the simpler set

$$\nabla \cdot \vec{v}^* = 0$$

$$\frac{\partial \vec{v}^*}{\partial t^*} + \vec{v}^* \cdot \nabla \vec{v}^* = -\frac{\nabla p^*}{\rho_0} + \nu \nabla^2 \vec{v}^* + \vec{g} - \beta(T^* - T_0)\vec{g} \qquad (1)$$

$$\frac{\partial T^*}{\partial t^*} + \vec{v}^* \cdot \nabla T^* = \frac{k}{\rho_0 c_p} \nabla^2 T^*$$

where starred symbols denote physical quantities. These equations are conventionally nondimensionalized with length scale d and time scale d^2/χ, where $\chi = k/\rho_0 c_p$ is the thermal diffusivity. The final equations of motion in nondimensional form with the hydrostatic part eliminated are

$$\nabla \cdot \vec{v} = 0$$

$$\frac{\partial \vec{v}}{\partial t} + \vec{v} \cdot \nabla \vec{v} = -\nabla p + Pr\, \nabla^2 \vec{v} + Ra\, Pr\, \theta \vec{e} \qquad (2)$$

$$\frac{\partial \theta}{\partial t} + \vec{v} \cdot \nabla \theta = \nabla^2 \theta$$

The velocity is scaled by χ/d, the pressure by $\rho_0(\chi/d)^2$, and the temperature change θ by the driving temperature difference ΔT. The unit vector $\vec{e}$ is positive upward. Two key parameters appearing as coefficients are the Prandtl number ($Pr = \nu/\chi$) and the Rayleigh number ($Ra = \beta g \Delta T d^3/\nu\chi$). In all the present computations it is assumed that the medium is air with $Pr = 0.71$.

The linear perturbation equations are obtained from equation (2) by considering deviations from a basic state consisting of $\vec{v} = 0$ and $\theta = 1 - y$, where $y = 0$ is the base of the cavity and $0 \le (x,y) \le 1$.

$$\nabla \cdot \vec{v}' = 0$$

$$\frac{\partial \vec{v}'}{\partial t} = -\nabla p' + Pr\, \nabla^2 \vec{v}' + Ra\, Pr\, \theta' \vec{e} \qquad (3)$$

$$\frac{\partial \theta'}{\partial t} = \nabla^2 \theta' + \vec{v}' \vec{e}$$

The primed quantities in equation (3) are equivalent to those unprimed in equation (2) except for the temperature, which is related by $\theta = \theta' + (1 - y)$. These equations must be augmented with appropriate boundary conditions. The linear system represented by equation (3) is an eigenvalue problem and, unlike the full equations, it is solved with homogeneous boundary conditions.

Numerical Method

In two dimensions, equation (2) is a system of four partial differential equations for the dependent variables (u,v,θ,p). The pressure plays a special role in the incompressible Navier-Stokes equations as the enforcer of mass conservation. If only those dependent variables with explicit time derivatives are retained, the following system of homogeneous matrix partial differential equations is obtained:

$$\frac{\partial \vec{U}}{\partial t} + A\frac{\partial \vec{U}}{\partial x} + B\frac{\partial \vec{U}}{\partial y} + C\frac{\partial^2 \vec{U}}{\partial x^2} + D\frac{\partial^2 \vec{U}}{\partial y^2} + E\vec{U} = 0 \qquad (4)$$

where $\vec{U}$ is a three-component solution vector consisting of (u,v,θ), A = diag (u,u,u), B = diag(v,v,v), C = D = diag (–Pr,–Pr,–1), and $E = -Ra\, Pr\, \delta_{23}$. The first-order terms represent convection, the second-order terms diffusion, and the last is a body-force coupling the momentum and energy equations. The finite-difference algorithm is defined by examining the way that plane waves are processed by equation (4). The "ansatz" is a plane wave with arbitrary wave number k,l of the form $\vec{U} = \vec{Y}(t)\, e^{ikx+ily}$, which is similar to that used in asymptotic wave theory (Whitham (1974)). Substituting $\vec{U}$ into equation (4) yields a first-order matrix ordinary differential equation for the amplitude function Y(t).

$$\frac{d\vec{Y}(t)}{dt} + ikA\vec{Y}(t) + ilB\vec{Y}(t) - k^2\, C\vec{Y}(t) - l^2\, D\vec{Y}(t) + E\vec{Y}(t) = 0 \qquad (5)$$

with a formal solution in terms of matrix exponentials:

$$\vec{Y}(t) = \vec{Y}_0 \exp\left(-\int kA\,dt + ilB\,dt - k^2C\,dt - l^2D\,dt + E\,dt\right) \quad (6)$$

The basis of the algorithm is to consider the change in $\vec{Y}$ over a small time interval τ where temporal changes in the coefficient matrices are ignored. If a mesh parameter h and the ratio $p = \tau/h$ is introduced, the integral is replaced by a product of matrix exponentials in terms of nondimensional spatial measures kh and lh. The wave parameter kh (or lh) will play a fundamental role in the construction of finite-difference molecules. A significant challenge in deriving finite-difference algorithms is to maintain solution accuracy as kh (and lh) varies over the allowable range $(0,\pi)$. Complete resolution is not possible as there will always be numerical artifacts leading to phase or amplitude distortion at short wavelengths. The goal of this effort is to derive formulas of maximum accuracy for a given stencil in space-time.

For convenience, the vectors $\vec{Y}_0$ and $\vec{Y}$ are replaced by the conventional $\vec{U}^n$ and $\vec{U}^{n+1}$ to represent the solution vector at sequential time steps. The solution is put in the special form

$$\vec{U}^{n+1} = e^{D\tau/h^2\, l^2h^2} e^{C\tau/h^2\, k^2h^2} e^{-E\tau} e^{-iBp\, lh} e^{-iAp\, kh} \vec{U}^n \quad (7)$$

Several approximations have been made in the process of deriving this fundamental formula. First, the coefficient matrices A, B, etc. are assumed locally constant. Second, splitting the exponential into a product of terms is strictly valid for scalar arguments or matrices with special properties. Both approximations would indicate a drop to first-order accuracy in the worst case. However, it is argued that an essential criterion of these simulations is to maintain adequate phase resolution in the individual one-dimensional algorithms serving as the components of equation (7).

Each term in equation (7) is interpreted as an incremental one-dimensional operator on $\vec{U}^n$ that gradually evolves the solution vector to $\vec{U}^{n+1}$. The analogy with locally one-dimensional waves is complete when one considers the simple scalar wave operator $\partial u/\partial t + a\partial u/\partial x$ with an input harmonic wave $e^{i\omega t + ikx}$. In this case $u^{n+1} = e^{-icn\,kh} u^n$ (from the dispersion relation $\omega + ka = 0$ and the Courant number $cn = a\tau/h$). Only one scalar operator is required to find u^{n+1} from u^n. With reference to equation (7), the matrix exponentials are replaced by partial solutions in a sequence of implicit finite-difference matrix operators:

$$\vec{U}^{n+1} = \mathcal{D}^{(y)}\, \mathcal{D}^{(x)}\, \mathcal{P}\mathcal{R}^{(0)}\, \mathcal{C}^{(y)}\, \mathcal{C}^{(x)} \vec{U}^n \quad (8)$$

The solution sequence is a serial operation involving $\vec{U}^{(1)} = \mathcal{C}^{(x)}\vec{U}^n$, $\vec{U}^{(2)} = \mathcal{C}^{(y)}\vec{U}^{(1)}$, etc. Each term has an obvious counterpart in equation (7) except for the inclusion of the pressure operator $\mathcal{P}$. The six-step process involves two convection sweeps, two diffusion sweeps, a velocity-temperature coupling, and a pressure computation.

Numerical dispersion can introduce errors of a subtle nature; these errors are most apparent in wave problems. The nature of these effects and the associated waveform distortion effect using an acoustics model is discussed in Davis (1991). Numerical dispersion of nonlinear weakly dissipative systems is very difficult to isolate when all other interrelated physical effects are considered. However, accurate modeling of the convective terms is critical to long-time solution accuracy. The procedure adopted is discussed in the previously cited reference where a discrete dispersion relation approach is used to obtain the best possible approximation for the chosen stencil. The ability of the algorithm to track accurately a range of wavelengths is also demonstrated in the cited reference. Boundary values for convection are computed from incoming and outgoing radiation conditions. It should be noted that these intermediate velocities do not satisfy the no-slip conditions. The complete convection algorithm is presented in the appendix.

The coupling term is treated in a simple manner. Unlike the previous operators, only the local solution at (x,y) is required to advance to the next time level. Since no derivatives are involved, the updated solution $\vec{U}^{(3)}$ is obtained from a Taylor series expansion of the matrix exponential $e^{E\tau}$ to second order. The matrix E contains only one off-diagonal element, as indicated above.

The pressure is introduced as a constraint to enforce mass conservation. Chorin (1968) first proposed an approach (which is now well accepted) to define a pressure term from the local velocity gradient by $\vec{v}^{(4)} - \vec{v}^{(3)} = -\tau\,\nabla p$ so that p satisfies a Poisson equation $\nabla^2 p = \nabla \cdot \vec{v}^{(3)}/\tau$ from the continuity condition $\nabla \cdot \vec{v}^{(4)} = 0$. This divergence is computed using second-order central differences and the pressure computed from an available Poisson solver. Boundary conditions are imposed from the condition that the normal velocity $\vec{v}^{(4)}$ vanishes on all four walls.

The diffusion operator is treated with an algorithm of the Crank-Nicolson form. Actually, the most accurate computational molecule on a 3-point stencil is of order (t^2, h^4) in contrast to the Crank-Nicolson molecule, which is of order (t^2, h^2). This algorithm also appears in the literature,

and it is referred to as the Douglas formula. (See Mitchell (1969).) However, the Crank-Nicolson formula was found to be adequate for the range of physical phenomena in this study. Diffusion is the last operation in the six-step process; it allows the imposition of no-slip boundary conditions. These algorithms are also shown in the appendix.

The solution sequence is chosen in order to address the problem of intermediate boundary conditions in a physically meaningful manner. The boundary conditions for convection are set by the operator itself. The coupling term causes no special boundary-condition problem since no neighboring mesh points are involved. The pressure plays a dual role of enforcing the conservation of mass and causing the *normal component* of boundary velocity to vanish.

At this stage, an inviscid solution (the Euler equation) is available. The tangential velocity at the wall is a measure of the incremental wall vorticity strength at the indicated time step. The final diffusion sweeps define the viscosity-induced shear and enable all boundary conditions to be imposed exactly. During this final step the initially solenoidal velocity field remains solenoidal; this characteristic is a fundamental property of the heat equation.

Solutions were obtained on a uniform 25×25 mesh with a time step chosen from $\tau = 0.06h$. There is no externally imposed velocity scale, but a Courant number $U\tau/h$ based on the final maximum convective velocity ranges to about one. These time steps are higher than usual since the convection algorithm is dissipation free and dispersion is low enough to minimize phase errors. The basic convection finite-difference molecule is phase accurate to a Courant number of about two, but dependent-variable coupling in the Boussinesq equations reduces its practical limit to a Courant number of about one. A typical 400-step run to steady flow takes about 90 seconds(s) on a Cray Y-MP.

Numerical Solutions

The initial-boundary-value problem is shown in figure 1. The side walls are rigid and insulated to the flow of heat. The top and bottom walls are also impervious, but they are maintained at prescribed temperatures. Motion is initiated from rest by a unit step in temperature that causes a large energy input which induces a transient flow that evolves into a final steady-state pattern. This pattern can be either convecting or conducting, depending on Rayleigh number. This indicial approach is both physically plausible and firmly rooted in classical linear system theory. The temperature boundary condition on the lower wall is modeled with a "noisy heater;" that is, the

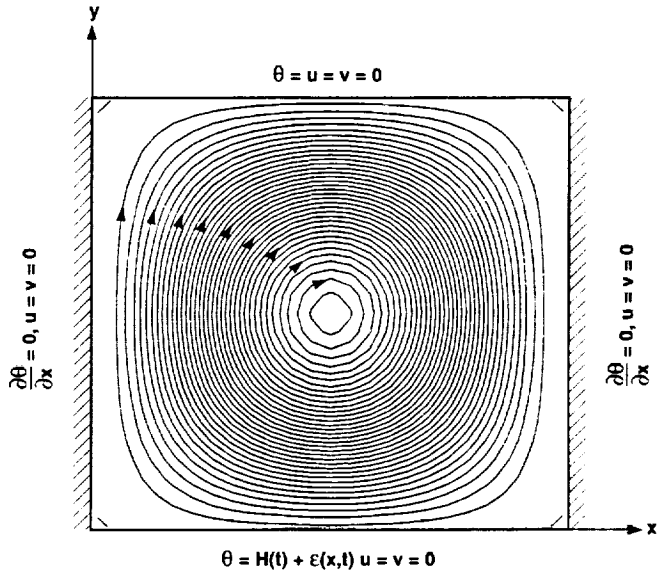

Figure 1. Geometry and typical flow pattern for natural convection in a box.

temperature $1 + \varepsilon(x,t)$ is considered to vary randomly in time ($t > 0$) with a prescribed space dependence.

The response of a stable physical system governed by linear homogeneous equations is an exponential decay to an equilibrium rest condition. The most significant parameter is its time constant. The situation for nonlinear systems is not as simple. The possibility of multiple steady solutions and bifurcation phenomena can easily be appreciated with the simple Ginzburg-Landau model considered by Rosenblat and Davis (1979). Solutions to the nonlinear model evolution equation

$$\frac{dU}{dt} = (R - 4)\,U - U^3$$
$$U(0) = U_0 \qquad (9)$$

are shown in figure 2(a) for a sequence of initial conditions U_0. If $R = 2$ (left panel), a value less than the critical $R_c = 4$, the step response decays exponentially for any choice of initial conditions. When $R = 6$ (right panel), any disturbance ultimately resolves itself into the preferred steady solution $U(\infty) = \pm 1.414$. If negative values of U are permitted, this is an example of a symmetric (pitchfork) bifurcation, the positive branch of which is depicted in figure 2(b). The branch $U = 0$ is unstable to infinitesimal perturbations if $R > 4$.

The Rayleigh-Benard system can be interpreted in the spirit of the Ginzburg-Landau model with a global kinetic energy measure $U(t) = \iint \frac{1}{2}\,\vec{v}\cdot\vec{v}\,dA$. If $Ra < Ra_c$, U(t)

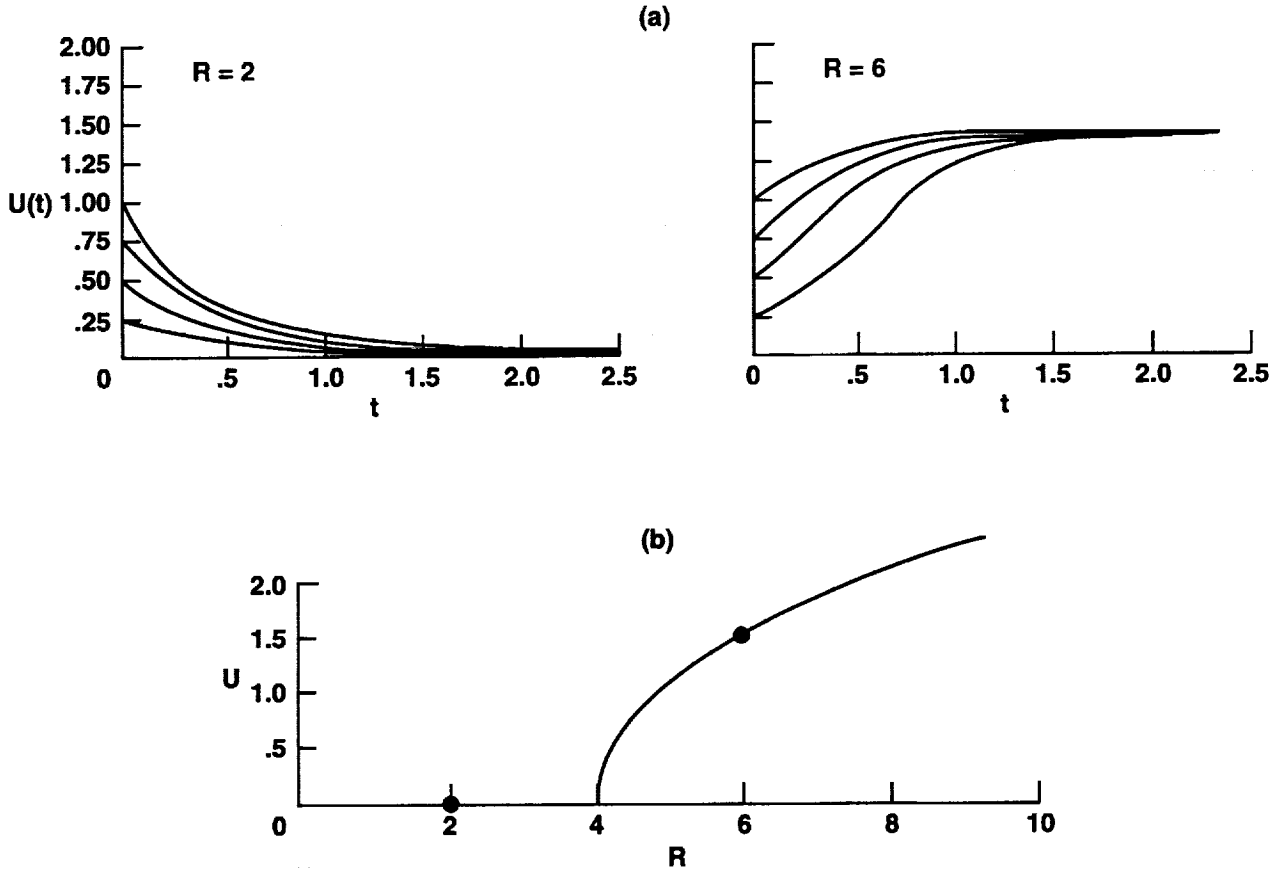

Figure 2. Response of a model nonlinear system to step inputs of 0.25, 0.50, 0.75, and 1.00. (a) System time history for subcritical (left) and supercritical (right) values of parameter R. (b) Bifurcation diagram of model nonlinear system.

should decay exponentially whereas bifurcations will occur at supercritical Rayleigh numbers. The nature of Rayleigh-Benard instability is shown in figure 3, which depicts computations of U(t) on a semilog scale from numerical solutions of equation (2) with Ra as parameter. At the initial instant of motion the temperature step induces a uniform buoyant upflow that decays because of viscous stresses in the cavity and at the side walls. At a critical Rayleigh number buoyancy forces overwhelm dissipation causing exponential growth in U. At the critical Rayleigh number the growth is very slow and of long duration. There are four significant parameters relating to these curves: the onset time for growth, the growth rate, the time to nonlinear saturation, and the amplitude of the final state.

This response is contrasted to linear perturbation theory that predicts the growth rate (eigenvalues) and some idea of the final state (the eigenfunctions). The linear solution is of the form $e^{\alpha t} f(x,y)$ where α is the eigenvalue and $f(x,y)$ is its eigenfunction. This type of instability is known as absolute or global instability; it is illustrated in figure 4, which shows the time history of U from solutions of equation (3) as dashed lines. Three Rayleigh numbers are chosen and are superimposed on the related nonlinear solution from equation (2). Starting with a short transient, the curves representing solutions of the linear equations quickly assume exponential form and become unbounded in time. The exponential-growth portions of the curves are well predicted, but other significant parameters are left unresolved when linear theory is used.[1]

The growth rate α was extracted from the perturbation solutions, and it is shown in figure 5 by the curve labeled "mode 1." The interpolated value of Rayleigh number Ra

[1]In the analysis of transition on airfoils and wings using linear stability theory an attempt to predict transition is often made based on the so-called "e-to-the-N-method." This empirical procedure predicts the distance from instability to transition by assuming an amplitude growth ratio of e^N where N is about 10. This procedure is clearly analogous to the use of linear theory in figure 4 to predict the nonlinear saturation value.

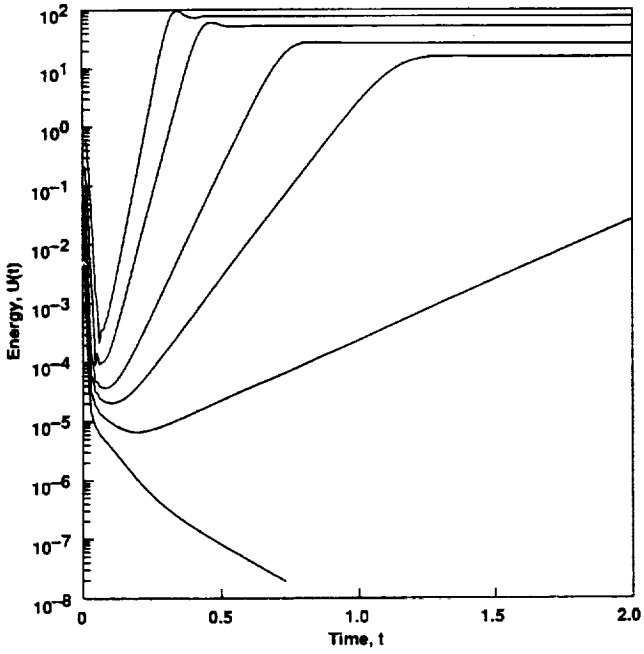

Figure 3. Global behavior of Rayleigh-Benard system for Rayleigh numbers 2000, 3000, 4000, 5000, 7500, and 10,000.

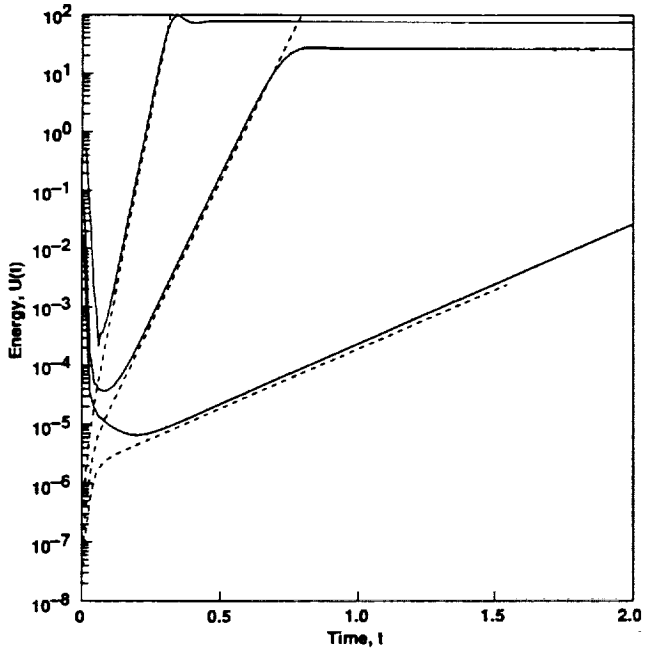

Figure 4. Superposition of linear (- - - - -) and nonlinear (_____) response curves of the Rayleigh-Benard system for Rayleigh numbers 3000, 5000, and 10,000.

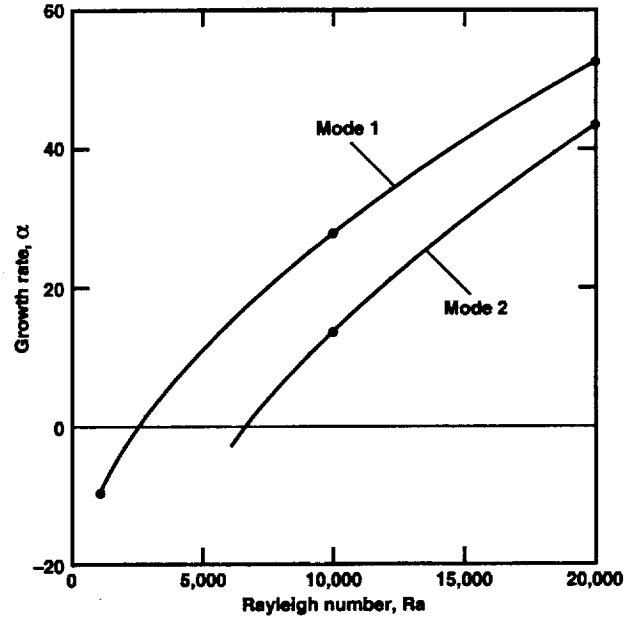

Figure 5. Curves of growth rate as a function of Rayleigh number for rotating (mode 1) and co-rotational (mode 2) eigenfunctions. Solid lines: 25 x 25 mesh, symbols: 50 x 50 mesh.

at instability onset is 2512, which compares favorably with the values 2553 and 2585 reported by Lee et al. (1989) and Kurtzweg (1965), respectively. Numerical experiments with the perturbation equations revealed another instability mode that was only excited with perturbations that were symmetric with respect to the line x = 0.5. The growth rates of this mode (mode 2 in the figure) are smaller than those of mode 1 and they become positive beyond a second critical Rayleigh number $Ra_{cc} = 7017$. Selected computations with a doubled grid are shown with filled symbols in figure 5. The eigenfunctions associated with each eigenvalue are obtained from the evolving numerical solution. During exponential growth they are simple multiples of one another. Figure 6 shows computed linearized eigenfunctions for temperature and velocity corresponding to modes 1 and 2. (The temperature eigenfunctions are defined as deviations from a purely conducting linear state.)

Steady-state solutions of the nonlinear equations may be represented on a bifurcation diagram such as that shown in figure 7. Here, the square root of steady-state kinetic energy is taken as a representative amplitude. These equilibrium modes are computed by using initial conditions with the same symmetries as the linear eigenfunctions. Modes 1 and 2 are almost exact fits to the interpolating parabolas $0.1076\sqrt{Ra-2512}$ and

Mode 1 Eigenfunctions

Perturbation temperature **Velocity vectors**

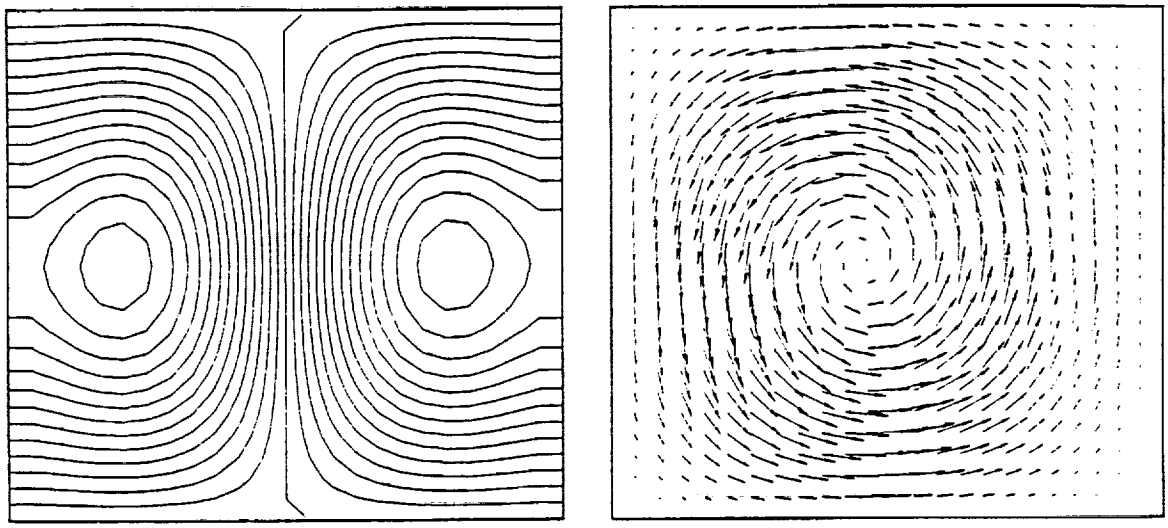

Mode 2 Eigenfunctions

Perturbation temperature **Velocity vectors**

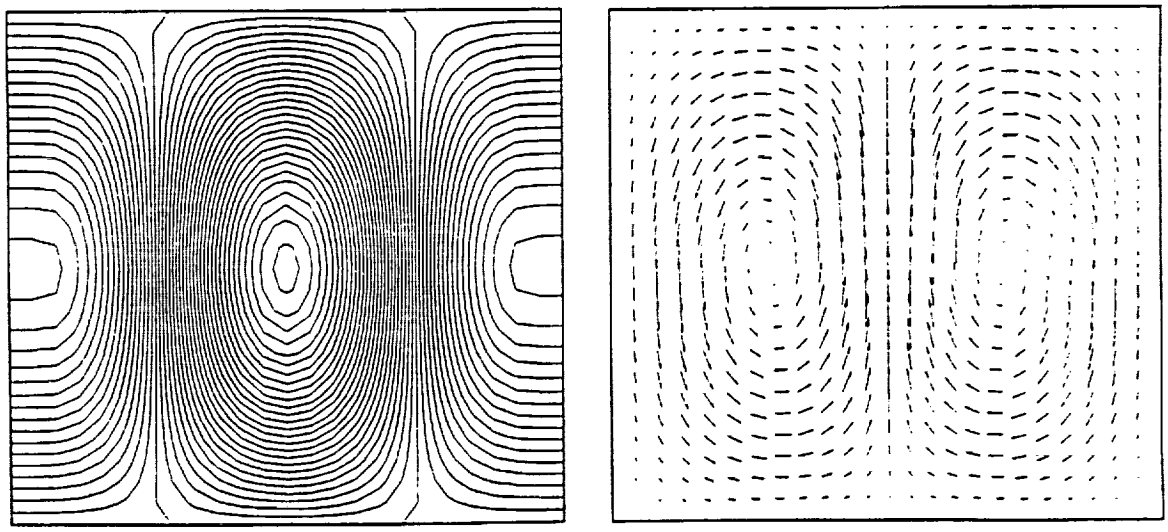

Figure 6. Maps of modes 1 and 2 eigenfunctions from solution of linear perturbation equations. 25 × 25 mesh, Ra = 7500.

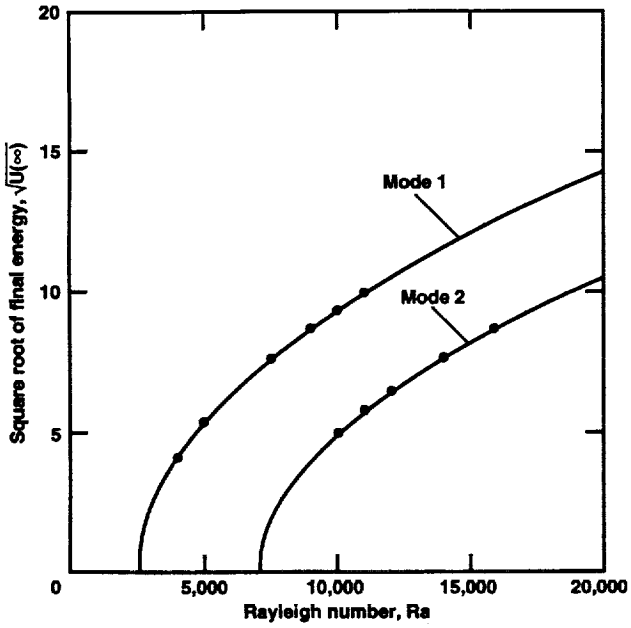

Figure 7. Finite-amplitude states for the Rayleigh-Benard system. 25 x 25 mesh, Ra = 7500. Symbols: computation, solid lines: best-fit parabolas.

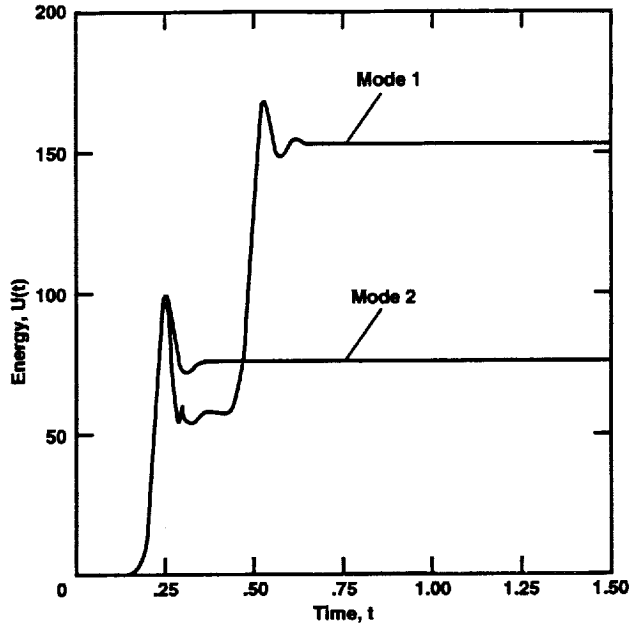

Figure 8. Time evolution of global parameter U showing selection of mode 1 and mode 2 final states. 25 x 25 mesh, Ra = 16,000.

$0.09176\sqrt{Ra-7017}$. These results are consistent with Landau's analysis of nonlinear absolute stability (Landau and Lifshitz (1959), p. 104): they predicted that the amplitudes of the equilibrium state will be proportional to the square root of the deviation of Ra from the critical value. These results show that the numerical algorithm predicts both linear and nonlinear effects that are entirely consistent with the accepted behavior of such flows.

In the next series of calculations the case Ra = 16,000 will be considered in some detail in order to distinguish the possible stable states associated with the linear eigenfunctions and the role of the boundary conditions in selecting each state. Two bifurcation curves were identified in figure 7 as being representative of stable equilibrium states. The first is a unicellular vortex motion bifurcating from Ra = 2512 with an amplitude measure of 12.4, and the second a symmetric mode bifurcating from Ra = 7017 with an amplitude measure of 8.7.

A series of runs at Ra = 16,000 starting from rest with a small random 1% temperature perturbation on the base of the cavity showed evidence of both modes. The vortex modes (either clockwise or counterclockwise rotation) appeared more than twice as often as the two-vortex configuration. Energy growth curves (on a linear scale) are shown in figure 8. There seemed to be some indecision just after the exponential-growth phase as to which mode would predominate. In fact, this case shows that the mode 1 solution coincides with the mode 2 growth-rate path at early times. The final state for both modes is presented in figure 9, with panels of perturbation temperature, total temperature, and velocity vectors. These modes retain remnants of the linear eigenfunctions of figure 6, but they are distorted by the nonlinear convection term in the Navier-Stokes equation.

Examination of the transient motion shows that the nonlinear stability curves possess a characteristic energy dip (cf. fig. 3) where many significant events occur. In this region the flow first aligns itself into the preferred spatial pattern (an "immature eigenfunction") in preparation for exponential growth. The field of velocity vectors is examined at the six points indicated at the top of figure 10. The first three represent the internalization period of the initial conditions (also called "receptivity"), the fourth the minimal energy state, and the last two the instability mode that determines the final state.

A generally uniform updraft in figure 10(a) is the initial response to the temperature step function; the large shear generates side-wall vorticity. The velocity terms in the Navier-Stokes equation convect and diffuse this vorticity, but the pressure plays a special role. In enforcing continuity, it tends to turn or rotate the flow. The net effect, along with the no-slip boundary conditions, is to generate two narrow recirculating eddies as shown in figure 10(b). The vortices migrate from the wall and align themselves more

Mode 1 Solution

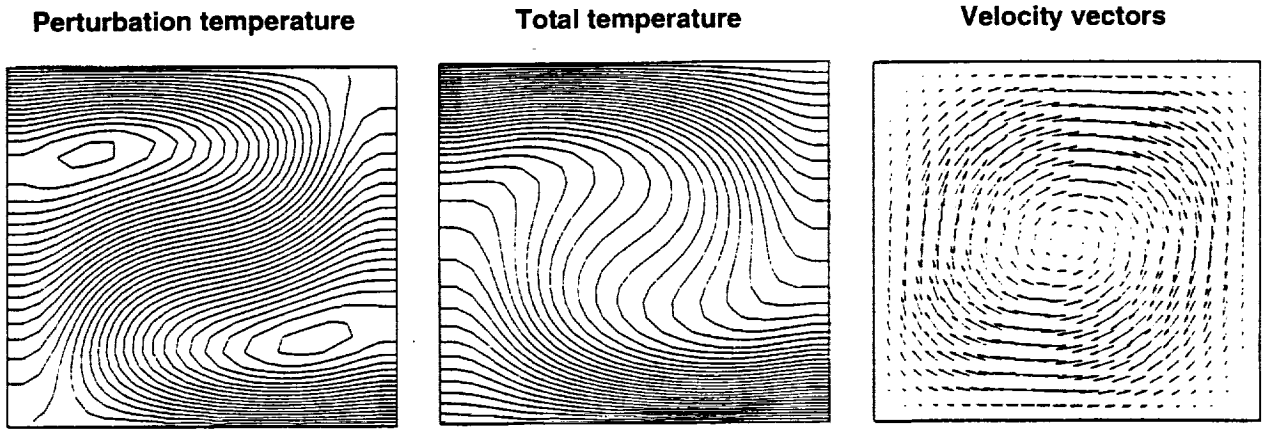

Mode 2 Solution

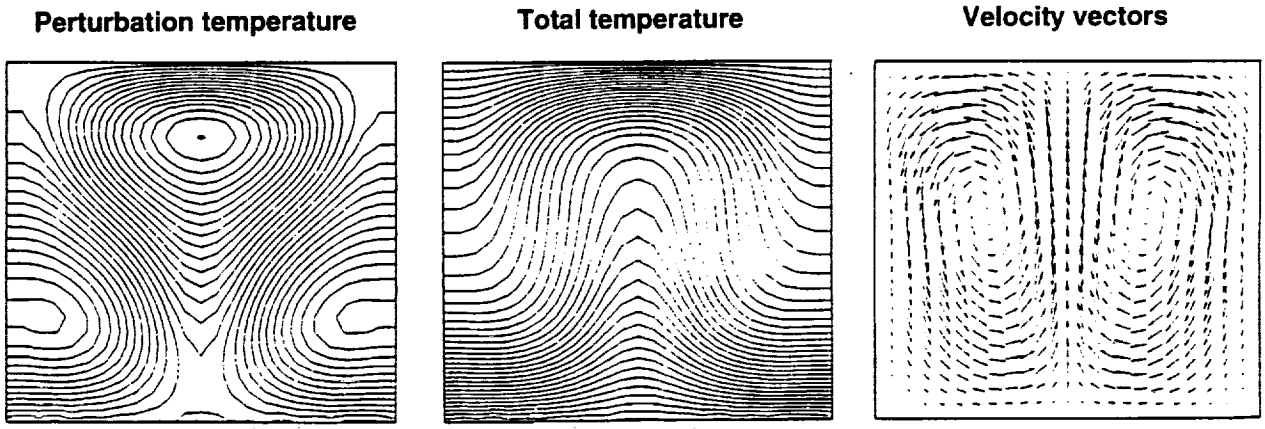

Figure 9. Maps of mode 1 and 2 final states. 25 × 25 mesh, Ra = 16,000.

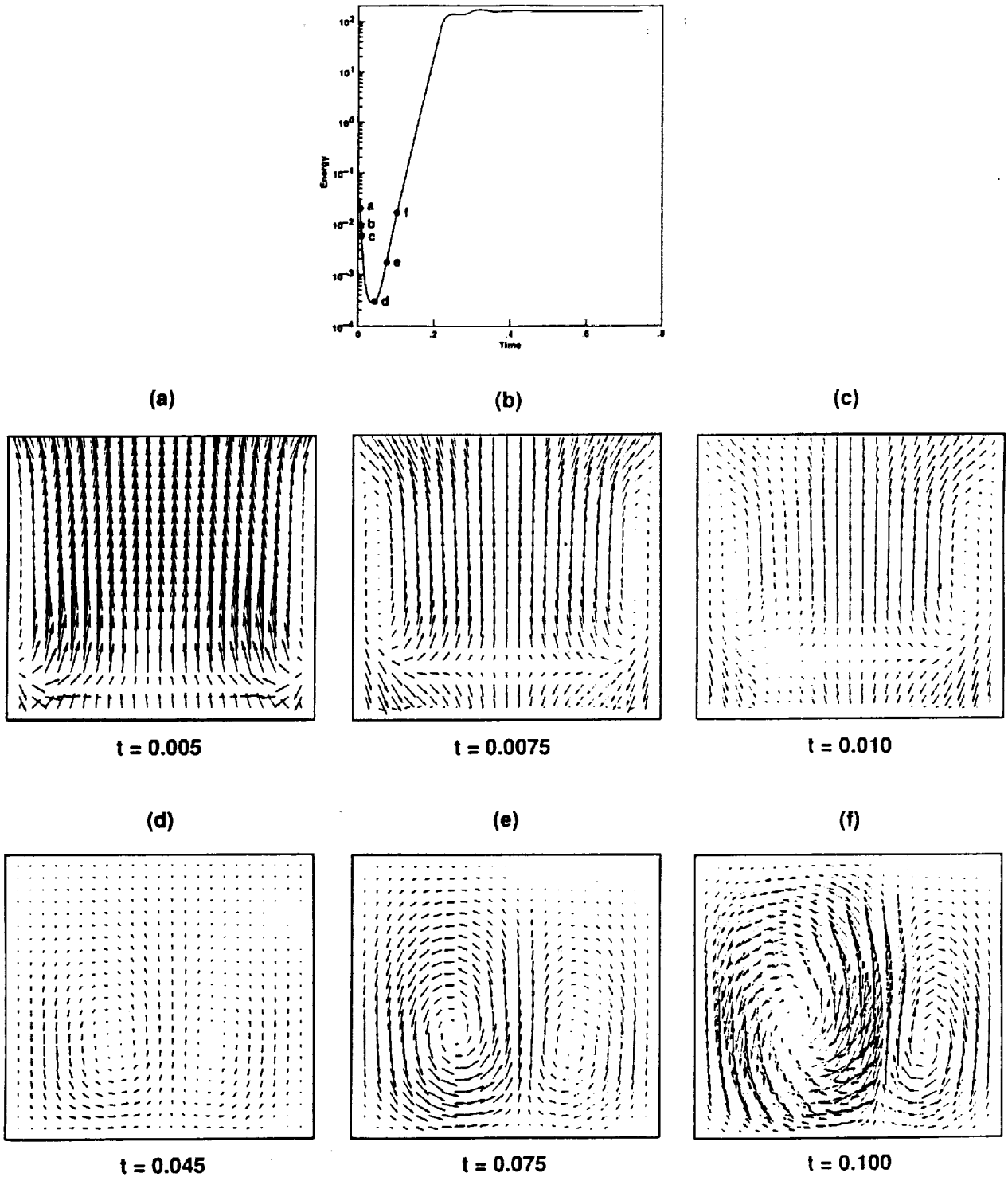

Figure 10. Velocity-vector maps showing internalization of disturbances and reconfiguration for instability growth at six instants of time.

or less symmetrically in the manner of a mode 2 eigenfunction as in figure 10(c). This spatial realignment takes place in a field of decreasing energy. (All velocities in fig. 10 are to the same scale.) The flow is now configured for unstable growth. The small, random, 1% temperature perturbations on the lower boundary buffet the eddies about, and a chance push in the right direction induces exponential growth. Panel 10(d) shows the point at which these disturbances first start to affect the flow and panels 10(e) and 10(f) confirm the dominance of the left vortex. This counterclockwise eddy soon extinguishes its partner and the final state will consist of a single large vortex.

Some investigations into what we have called the "symmetric state" are shown in figures 11 and 12. Unlike previous examples, the flow is first established as the symmetric two-vortex mode before disturbances are imposed. Disturbances are initiated at t = 0.5 and released at t = 0.6. Three types of temperature distributions along the bottom wall are chosen:

$$\begin{aligned} &\text{(a) } \theta(x) = \varepsilon\, \text{Rand}\{-1,1\}\,(x - 0.5) \\ &\text{(b) } \theta(x) = \varepsilon \\ &\text{(c) } \theta(x) = \varepsilon\,(x - 0.5) \end{aligned} \qquad (10)$$

where Rand{−1,1} is a random number in the indicated range. The disturbances (a) have no spatial coherence while disturbances (b) and (c) are symmetric and antisymmetric, respectively, with respect to the vertical line of symmetry x = 0.5. Figure 11 indicates that random perturbations with peak-to-peak amplitudes as much as 100% cause the two vortices to react quite violently with one another but do not change the fundamental modal structure, which settles down to its initial configuration. Symmetric disturbances of type (b) cause violent excursions, but they also fail to upset the basic symmetry. Case (c) of equation (10), presented in figure 12, shows that above a critical amplitude the flow becomes asymmetric and evolves into the stable vortex mode state. In summary, 1) the symmetric state is stable to symmetric disturbances of any size, 2) the symmetric state is stable to small antisymmetric or random disturbances, and 3) the symmetric state is unstable to larger antisymmetric disturbances.

The mode selection process will now be investigated with the aid of a model second-order nonlinear dynamic system. Consider a phase-plane (or state-space) representation with the kinetic energy U(t) as ordinate and dU/dt as abscissa. The instantaneous state actually requires an infinite-dimensional velocity vector, but U will represent a convenient measure for a model second-order damped nonlinear oscillator. Finite-amplitude steady flows consist of discrete limit points on the $\dot{U} = 0$ axis. At supercritical

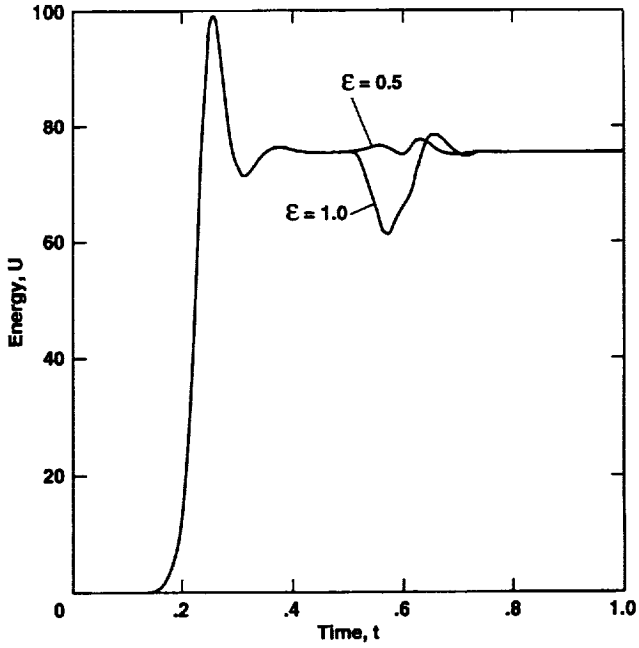

Figure 11. Energy time history for random temperature inputs to base of cavity during time interval 0.5 - 0.6 with various amplitudes.

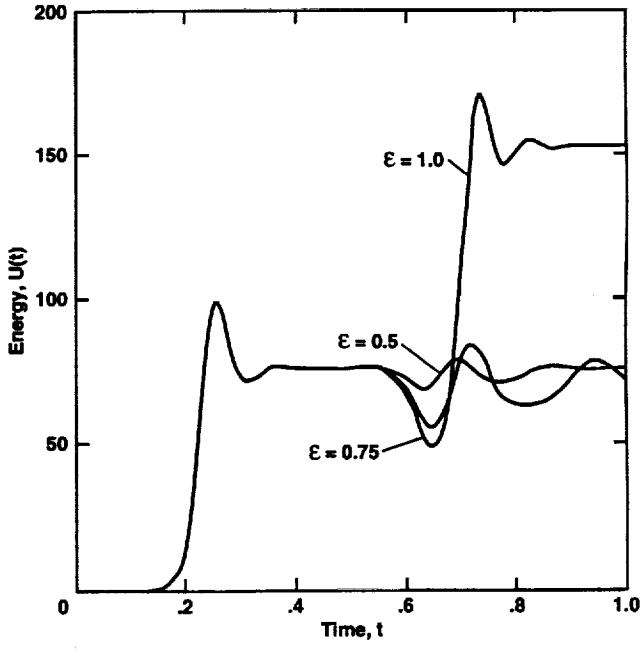

Figure 12. Energy time history for anti-symmetric temperature inputs to base of cavity during the time interval 0.5 - 0.6 with various amplitudes. Ra = 16,000.

Rayleigh numbers there may be many limit points: singularities possessing domains of attraction to which all solution paths congregate. Figure 12 shows that there are attractors at U = 76 and U = 154 for Ra = 16,000. The state-space path corresponding to $\varepsilon = 1$ is shown in figure 13 to be attracted from rest to the mode 2 state at A and then perturbed to a path that encroaches on the mode 1 domain of attraction. Points A and B along the path correspond to the imposition and elimination of the disturbance at t = 0.5 and t = 0.6. The curve beyond point B is the response of the Boussinesq equations to initial conditions at B that were vigorous enough to propel the solution path away from the mode 2 attractor.

The stable state that will be realized depends on the value of the parameter ε; there must be a critical amplitude depending on ε that separates these flows. The particular path corresponding to this critical value should pass through a saddle-type singular point in the phase plane. Numerical experiments using the bisection method identified critical amplitude bounds in the range $0.9031 < \varepsilon < 0.9047$. State-space trajectories for four

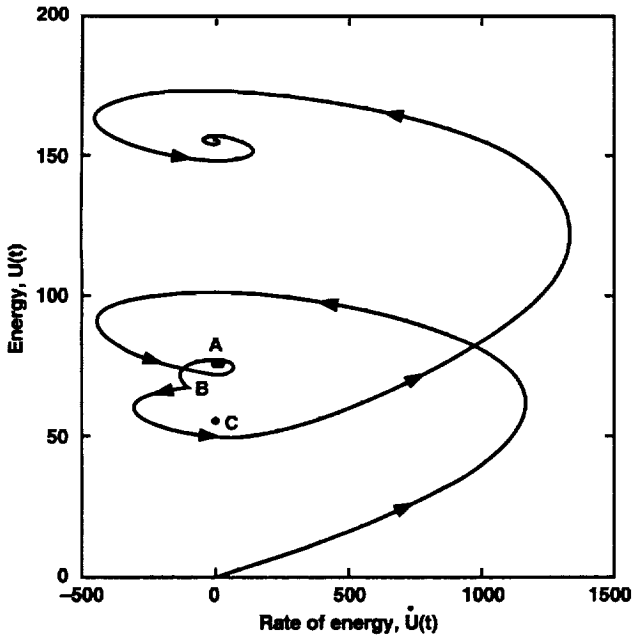

Figure 13. Phase-plane representation for flow evolving from rest to a mode 2 symmetric state at U = 76 and perturbed to a mode 1 state at U = 154 with anti-symmetric disturbances. Equation 10(c), $\varepsilon = 1.0$. The path moves below an unstable singular point at C.

amplitudes in the vicinity of the critical value are shown in figure 14. The trajectories pass near a singularity at point C, representing an unstable equilibrium. The role of this unstable state is appreciated from the time histories in figure 15 for $\varepsilon = 0.90312$ and $\varepsilon = 0.9047$. The system responds along a common path after removal of the perturbation at point B until it encounters the instability at U = 53.6; from here they evolve to a final state fated by the disturbance history. A change of 0.17% in ε induces a final state with an energy change of over 200%. A flow pattern near the unstable equilibrium point is shown in figure 16. Here the velocities prefer a diagonally symmetric pattern with vortices of opposite sense. The pattern for a sign-reversed flow near the instability point is similar except that vortices appear at opposite corners with sign-reversed flow.

The singular points of the trajectories shown in figures 13 and 14 do not line up in the usual stable-unstable-stable sequence because of the use of the positive-definite quantity U as the characteristic measure. A more conventional diagram can be recovered if a dependent variable that can be either positive or negative is selected as the characteristic measure. Figure 17 shows transient solution paths to the static attractors associated with the quantity $\Delta\theta$ (the temperature difference across the box at midheight). The sense of the single vortex solution can be positive or negative, as revealed by the symmetric location of the spiral attractors. The origin of this phase diagram represents both the initial conducting flow and the symmetric mode 2 state. The boundaries of the basins of attraction are defined by separatrices; they are approximately indicated by the solid lines, which represent trajectories for $\varepsilon = \pm 0.9047$. Representative paths in the two basins of attraction for positive $\Delta\theta$ are shown by dashed lines.

This digression to nonlinear dynamics for a specific disturbance mode and Rayleigh number is presented to illustrate how the numerical approach can be used to examine and interpret parametric trends with a global measure. A complete analysis of all possible modes, phase-plane parameters, and flow states is beyond the scope of this paper.

The examples discussed above for $Ra > Ra_{cc}$ have a richer structure than the response for $Ra < Ra_{cc}$ that allows only simple rotational-flow solutions. If the Rayleigh number is greater than about 20,000, fine-scale secondary instabilities appear and the role of three-dimensional disturbances and nonlinear oscillatory modes must be considered ab initio.

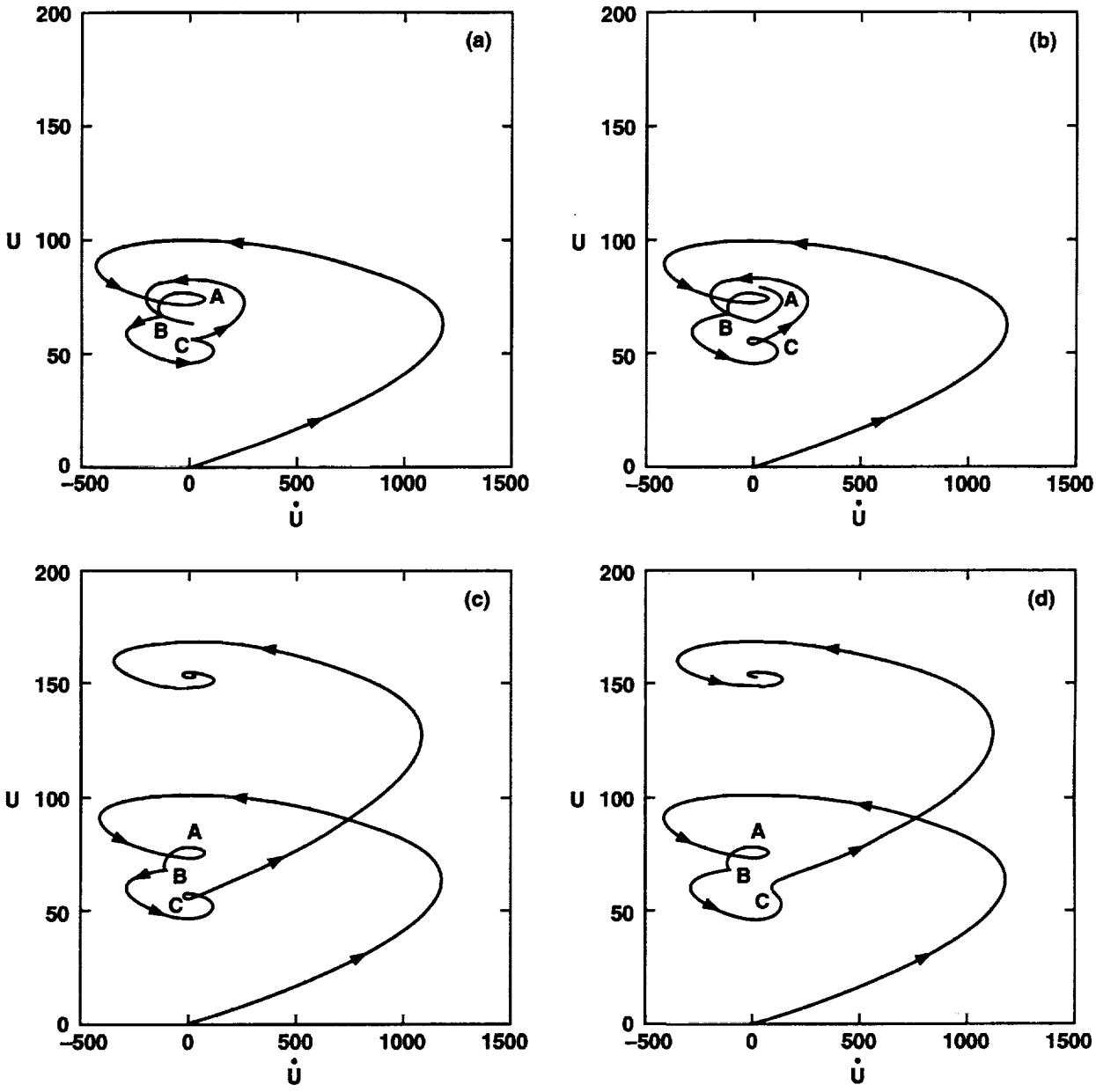

Figure 14. Phase-plane solution paths for disturbances that pass close to an instability point at C. (a) $\varepsilon = 0.9000$, (b) $\varepsilon = 0.90312$, (c) $\varepsilon = 0.90469$, (d) $\varepsilon = 0.91250$.

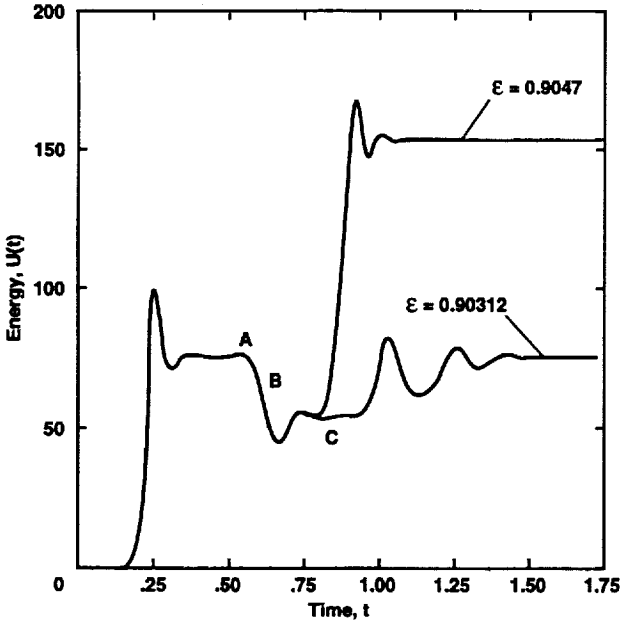

Figure 15. Energy time histories for amplitudes that pass near the unstable equilibrium.

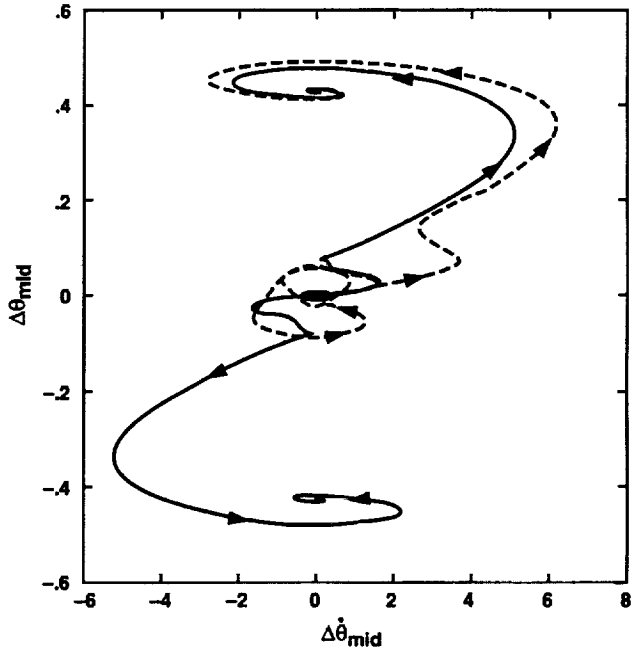

Figure 17. Phase-plane trajectories for solution paths using temperature differences across box at midheight.

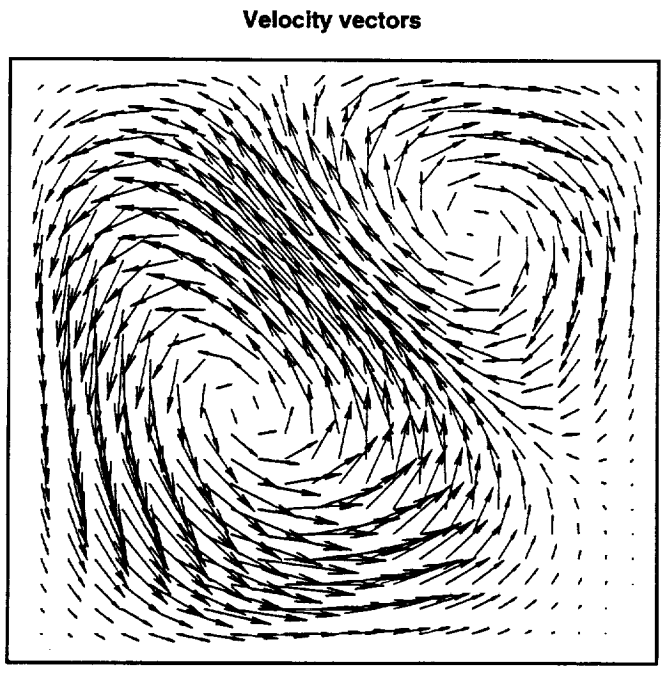

Figure 16. Velocity-vector maps in vicinity of unstable equilibrium at t = 0.8.

Conclusions

A new primitive-variable finite-difference simulation of the Boussinesq equations has revealed details of the initial-flow structure and has traced modes of instability from inception to the final nonlinear state. The finite-difference scheme used in these computations differs from other techniques in the use of matrix-exponential splitting to separate physical and dimensional processes. This method allows construction of efficient, low-dispersion computational molecules as well as relatively coarse meshes and longer time steps.

As a result of this study, a picture emerges of the response of the Boussinesq model to imposed disturbances. The initial response involves a realignment of the velocity field that is strongly influenced by the incompressibility constraint. Once the field attains a small but spatially coherent pattern, strong coupling with other dependent variables induces a rapid and large-scale change in the flow energy. Nonlinear effects cause saturation to a steady flow governed by the magnitude of the externally applied temperature field. While the linear perturbation equations can accurately predict the growth rates and eigenfunction patterns, the nonlinear equations must be analyzed in detail before the initial internalization process and the process of final pattern selection can be understood.

In this study only step-type motions—specifically instantaneously applied heating—have been used. Other initial conditions may have different initial responses, but the nature of instability growth will not change. In addition, only two-dimensional flows were considered. Expanding the parameter space to a third dimension and to other aspect ratios may invoke other interesting modes. The Boussinesq model of flow stability couples the dependent variables in a particular but relatively simple manner. Other models, especially those governing convective flows with inflow-outflow boundaries, will have other modal responses which will be investigated in the future using the numerical techniques introduced.

Appendix

Natural Convection Algorithm

The algorithm used to simulate the Boussinesq equations is presented schematically in equation (7). The procedure is similar to other time-splitting approaches except that each operator and each coordinate direction is identified as a separate physical process. It has been difficult to obtain accurate composite finite-difference formulas for convection and diffusion. However, simpler algorithms are obtained by separating the formulas into distinct steps. In this appendix the computational molecule for each step is shown in some detail.

The convection algorithm is split into separate x- and y-sweeps. The system is closed with finite-difference approximations to radiation conditions; this approach avoids the question of intermediate boundary conditions. Consider, for example, a uniform mesh at time $t = n\tau$ and points $x = (i-1)h$, $y = (j-1)h$ $(1 \le i, j \le N)$ with velocity denoted by $u^n_{i,j}$. A local Courant number is defined in terms of the local velocity by $cn = u^n_{i,j}\tau/h$. The algorithm for updating u at an interior mesh point during an x-sweep is:

$$\begin{aligned}
&\frac{1}{12}(cn-1)(cn-2)u^{n+1}_{i-1,j} - \frac{1}{6}(cn-2)\\
&\times(cn+2)u^{n+1}_{i,j} + \frac{1}{12}(cn+1)(cn+2)u^{n+1}_{i+1,j}\\
&= \frac{1}{12}(cn+1)(cn+2)u^{n}_{i-1,j}\\
&-\frac{1}{6}(cn-2)(cn+2)u^{n}_{i,j}\\
&+\frac{1}{12}(cn-1)(cn-2)u^{n}_{i+1,j}
\end{aligned} \qquad \text{(A1)}$$

The boundary algorithms at i = 1 and i = N are

$$\begin{aligned}
&(cn-1)u^{n+1}_{1,j} - (cn+1)u^{n+1}_{2,j} =\\
&-(cn+1)u^{n}_{1,j} + (cn-1)u^{n}_{2,j}\\
&-(cn-1)u^{n+1}_{N-1,j} + (cn+1)u^{n+1}_{N,j} =\\
&(cn+1)u^{n}_{N-1,j} - (cn-1)u^{n}_{N,j}
\end{aligned} \qquad \text{(A2)}$$

These sweeps convect the dependent variable in x without specific reference to the boundary conditions. If an arbitrary plane wave with wavenumber k is propagated through the mesh, equation (A1) is accurate to $(kh)^4$. Equation (A2) involves only two mesh points and it is accurate to $(kh)^2$. In the commonly used terminology, these equations are accurate in space-time to fourth- and second-order, respectively. This criterion is not a complete representation of the accuracy of the finite-difference approximation. In actual simulations the accuracy attainable with a given mesh depends on the gradients of the computed solution. In any physical problem a higher accuracy algorithm will always be a better choice, but it is more difficult to decide whether or not the computed solution is a more valid physical representation. The algorithm for v and θ is exactly the same as the preceding equations.

The y-sweep is computed in the same manner as equations (A1) and (A2) except that cn is now defined by $v^n_{i,j}\tau/h$ with the j index being variable. The notation $(n+1)$ does not mean that the solution bears any resemblance to the actual physical solution at time n + 1; it only denotes a partial correction as one step toward the ultimate physical solution.

The vector of dependent variables is now corrected for the coupling term involving the matrix E in equation (7). This term, which does not involve any spatial derivatives, is equivalent to the simple matrix equation $\partial \mathbf{U}/\partial t + \mathbf{E}\mathbf{U} = 0$. The updated vector is obtained from a Taylor series in time with τ as the small parameter:

$$\mathbf{U} = \mathbf{U}_0 e^{-\mathbf{E}\tau} = \mathbf{U}_0(\mathbf{I} + \mathbf{E}\tau + \frac{1}{2}\mathbf{E}\cdot\mathbf{E}\tau^2 + \ldots) \qquad \text{(A3)}$$

The matrix E is very simple; all powers of E vanish except for the first. The vertical velocity is updated from the simple formula

$$v^{n+1}_{i,j} = v^n_{i,j}(1 + E_{23}\tau) \qquad \text{(A4)}$$

Note that this revised velocity does not involve the solution at neighboring mesh points.

Updated velocities u, v are now available, and the pressure is computed in order that the velocities remain compatible with the incompressibility condition. The Poisson equation for p as discussed in the body of the paper is:

$$\nabla^2 p = \frac{1}{\tau}\left(\partial u/\partial x + \partial v/\partial y\right)$$
$$\frac{\partial p}{\partial x} = u, (x = 0, x = 1, 0 \le y \le 1) \qquad \text{(A5)}$$
$$\frac{\partial p}{\partial y} = v, (y = 0, y = 1, 0 \le x \le 1)$$

This two-dimensional elliptic boundary-value problem on a uniform mesh is solved with available software library routines. The solution for p is used to update the velocities from the defining equation

$$u_{new} = -\tau \partial p/\partial x + u_{old}$$
$$v_{new} = -\tau \partial p/\partial y + v_{old} \qquad \text{(A6)}$$

The last step is a diffusion to the final velocity as determined from a Crank-Nicolson sweep. In the x-direction:

$$-\frac{1}{2} dn\, u^{n+1}_{i-1,j} + (1 + dn)\, u^{n+1}_{i,j} - \frac{1}{2} dn\, u^{n+1}_{i+1,j}$$
$$= \frac{1}{2} dn\, u^{n}_{i-1,j} + (1 - dn)\, u^{n}_{i,j} + \frac{1}{2} dn\, u^{n}_{i+1,j} \qquad \text{(A7)}$$

where the diffusion number $dn = Pr\tau/h^2$ for velocity diffusion and $dn = \tau/h^2$ for temperature diffusion. The formula is exactly the same for y-diffusion. Boundary conditions based on the no-slip condition for velocity and either the no-slip or the no-flux condition for temperature are used.

Each of the tridiagonal equations appearing in these equations is solved by using variants of the Thomas algorithm. Although the diffusion equation is diagonally dominant and causes no solution difficulties, the Thomas algorithm will fail for equation (A1) if some of the local values of cn exceed unity. This failure is not due to the algorithm, which was shown in the cited references to be accurate to at least cn = 2, but it is caused by a breakdown in diagonal dominance required by the algorithmic construction. This breakdown forces the allowable time step to be reduced somewhat. Other classes of sparse matrix solvers that might alleviate this restriction are under investigation.

References

Busse, F. H.: Transition to Turbulence in Rayleigh-Benard Convection. Hydrodynamic Instabilities and the Transition to Turbulence, H. L. Swinney and J. P. Gollub, eds. Springer-Verlag, Berlin, 1981.

Chandrasekhar, S.: Hydrodynamic and Hydromagnetic Stability. Oxford, 1961.

Chorin, A. J.: Numerical Solution of the Navier-Stokes Equations. J. Computation, vol. 22, 1968, pp. 745-762.

Davis, S. S.: Low Dispersion Finite-Difference Methods for Acoustic Waves in a Pipe. J. Acoust. Soc. America, vol. 90, 1991, pp. 2775-2781.

Goldhirsch, I.; Pelz, R. B.; and Orszag, S. A.: Numerical Simulation of Thermal Convection in a Two-Dimensional Finite Box. J. Fluid Mech., vol. 199, 1989, pp. 1-28.

Kurtzweg, U. H.: Convective Instability of a Hydromagnetic Fluid within a Rectangular Cavity. Intl. J. Heat and Mass Transfer, vol. 8, 1965, pp. 35-41.

Landau, L. D.; and Lifshitz, E. M.: Fluid Mechanics, Pergamon Press, London, 1959.

Lee, N. Y.; Schultz, W. W.; and Boyd, J. P.: Stability of Fluid in a Rectangular Enclosure by Spectral Method. Int. J. Heat and Mass Transfer, vol. 32, 1989, pp. 513-520.

Mitchell, A. R.: Computational Methods in Partial Differential Equations. John Wiley & Sons, Inc., New York, 1969, p. 26.

Ogura, Y.; and Yagihashi, A.: On the Degeneracy of Finite-Amplitude Steady-State Solutions for Benard Convection in a Highly Truncated System. J. Meteorol. Soc. Japan, vol. 47, 1969, pp. 437-445.

Ogura, Y.: A Numerical Study of Wavenumber Selection in Finite-Amplitude Rayleigh Convection. J. Atm. Sci., vol. 28, 1971, pp. 709-717.

Rosenblat, S.; and Davis, S. H.: Bifurcation from Infinity. SIAM J. Appl. Math, vol. 37, 1979, pp. 1-19.

Saltzman, B.: Finite-Amplitude Free Convection as an Initial Value Problem. J. Atm. Sci., vol. 19, 1962, pp. 329-341.

Whitham, G. B.: Linear and Nonlinear Waves. John Wiley & Sons, Inc., New York, 1974.

REPORT DOCUMENTATION PAGE

Form Approved
OMB No. 0704-0188

1. AGENCY USE ONLY *(Leave blank)*	2. REPORT DATE	3. REPORT TYPE AND DATES COVERED
	May 1993	Technical Memorandum

4. TITLE AND SUBTITLE

Linear and Nonlinear Pattern Selection in Rayleigh-Benard Stability Problems

5. FUNDING NUMBERS

505-59-50

6. AUTHOR(S)

Sanford S. Davis

7. PERFORMING ORGANIZATION NAME(S) AND ADDRESS(ES)

Ames Research Center
Moffett Field, CA 94035-1000

8. PERFORMING ORGANIZATION REPORT NUMBER

A-93048

9. SPONSORING/MONITORING AGENCY NAME(S) AND ADDRESS(ES)

National Aeronautics and Space Administration
Washington, DC 20546-0001

10. SPONSORING/MONITORING AGENCY REPORT NUMBER

NASA TM-104007

11. SUPPLEMENTARY NOTES

Point of Contact: Sanford S. Davis, Ames Research Center, MS 260-1/260-A, Moffett Field, CA 94035-1000; (415) 604-4197

12a. DISTRIBUTION/AVAILABILITY STATEMENT

Unclassified-Unlimited
Subject Category – 34

12b. DISTRIBUTION CODE

13. ABSTRACT ***(Maximum 200 words)***

A new algorithm is introduced to compute finite-amplitude states using primitive variables for Rayleigh-Benard convection on relatively coarse meshes. The algorithm is based on a finite-difference matrix-splitting approach that separates all physical and dimensional effects into one-dimensional subsets. The nonlinear pattern selection process for steady convection in an air-filled square cavity with insulated side walls is investigated for Rayleigh numbers up to 20,000. The internalization of disturbances that evolve into coherent patterns is investigated and transient solutions from linear perturbation theory are compared with and contrasted to the full numerical simulations.

14. SUBJECT TERMS

Rayleigh-Benard stability, Numerical simulations, Nonlinear pattern selection

15. NUMBER OF PAGES

21

16. PRICE CODE

A02

17. SECURITY CLASSIFICATION OF REPORT	18. SECURITY CLASSIFICATION OF THIS PAGE	19. SECURITY CLASSIFICATION OF ABSTRACT	20. LIMITATION OF ABSTRACT
Unclassified	Unclassified		